chemosensors

MDPI

Article

Room-Temperature Environmental Gas Detection: Performance Comparison of Nanoparticle-Based Sensors Fabricated by Electrospray, Drop-Casting, and Dry Printing Based on Spark Ablation

Carlos Sánchez-Vicente [1], José Pedro Santos [1,*], Isabel Sayago [1], Vincent Mazzola [2] and Leandro Sacco [2]

[1] Nanosensors and Intelligent Systems (NoySI), Institute for Physical and Information Technologies (CSIC), 28006 Madrid, Spain; c.sanchez.vicente@csic.es (C.S.-V.); i.sayago@csic.es (I.S.)
[2] VSParticle B.V., Oostsingel 209, 2612 HL Delft, The Netherlands; v.mazzola@vsparticle.com (V.M.); l.sacco@vsparticle.com (L.S.)
* Correspondence: jp.santos@csic.es

Abstract: Chemical nanosensors based on tin dioxide (SnO_2) and zinc oxide (ZnO) nanoparticles (NPs) were developed and characterized for the detection of low concentrations of atmospheric pollutants, such as nitrogen dioxide (NO_2) and carbon monoxide (CO). The sensing layers were prepared using three fabrication methods: drop-casting, electrospray, and spark ablation coupled with an inertial impaction printer, to compare their performance. Multiple surface characterization techniques were carried out to investigate the surface morphology and elemental composition of the deposited layers such as SEM (scanning electron microscopy) and XPS (X-ray photoelectron spectroscopy) analyses. UV light photoactivation enabled the sensors to detect ultra-low concentrations of the target gases at room temperature (100 ppb NO_2 and 1 ppm CO). The measurements were conducted at 50% relative humidity to simulate real environmental conditions. All sensors were capable of detecting the target gases. Drop-casting is the simplest and most cost-effective technique, but it is also the least reproducible. In contrast, sensors based on the spark ablation technique achieved more homogeneous sensing layers, with practically no nanoparticle agglomeration, resulting in devices with lower noise and drift in their electrical response.

Keywords: gas sensors; ZnO; SnO_2; room temperature; pollutant gases; NO_2; CO; electrospray; drop-casting; spark ablation

check for updates

Received: 6 May 2025
Revised: 5 June 2025
Accepted: 13 June 2025
Published: 17 June 2025

Citation: Sánchez-Vicente, C.; Santos, J.P.; Sayago, I.; Mazzola, V.; Sacco, L. Room-Temperature Environmental Gas Detection: Performance Comparison of Nanoparticle-Based Sensors Fabricated by Electrospray, Drop-Casting, and Dry Printing Based on Spark Ablation. *Chemosensors* **2025**, *13*, 219. https://doi.org/10.3390/chemosensors13060219

Copyright: © 2025 by the authors. Licensee MDPI, Basel, Switzerland. This article is an open access article distributed under the terms and conditions of the Creative Commons Attribution (CC BY) license (https://creativecommons.org/licenses/by/4.0/).

1. Introduction

Growing concern about environmental pollution has intensified the search for new alternatives and technologies to monitor and control atmospheric pollutants. Gases such as NO_2 and CO are largely emitted by industrial and transportation activities, significantly impacting public health and the environment.

The current EU air quality directives, although useful, are less stringent than the recommendations of the World Health Organization (WHO). In 2020, exposure to NO_2, CO, and fine particles (PM2.5) contributed to hundreds of thousands of premature deaths in the EU. By 2030, the EU aims to reduce pollution-related premature deaths by 55% compared to 2005 levels through the implementation of pollution control programs and compliance with climate and energy targets [1,2].

In this context, traditional analytical methods such as gas chromatography–mass spectrometry (GC-MS) and Fourier transform infrared (FT-IR) spectrometry are not suitable

for massive deployment in dense measurement grids due to their high cost, bulky design, and the need for trained personnel to operate them [3]. Metal oxide semiconductor (MOS)-based gas sensors are a mature technology that has provided sensing solutions for decades due to their low cost, compact form, simple implementation, and high sensitivity in the ppm range toward multiple gas molecules [4]. Furthermore, the utilization of MOS at the nanoscale in at least one dimension has demonstrated the potential to outperform current commercial devices in terms of sensitivity and operational temperature [5]. These nanostructured materials have shown great potential for use as sensing layers for the detection of pollutant gases due to their properties, such as a high surface-to-volume ratio, high specific surface area, and a greater number of active surface sites. SnO_2 and ZnO are two of the most widely used metal oxides for resistive gas sensors due to their high sensitivity and good stability [6].

However, MOS-based sensors still face challenges related to selectivity and power consumption [7]. Currently, one of the main objectives in gas sensor research is to develop gas sensors that can operate at room temperature with improved performance and selectivity for different gaseous compounds [8]. Traditional resistive gas sensors incorporate heaters to warm the sensor membranes to temperatures between 100 and 500 °C. Operation at high temperatures can reduce the sensor's lifespan and stability, as well as increase the complexity of the substrate design and fabrication [9,10].

To enable these sensors to operate at room temperature, the sensing layer is illuminated with ultraviolet (UV) light, which can improve the material's conductivity by increasing the number of free carriers [11,12]. The light energy must be comparable to or greater than the bandgap of the semiconductor. In the case of SnO_2, it has a bandgap of 3.5 eV [13], while ZnO has a bandgap of 3.3 eV [6].

In addition to advances in these types of sensors, the development of small-sized, low-cost devices such as electronic noses would allow them to be installed in different locations, providing more comprehensive data. This, combined with advancements in Internet of Things (IoT) technology, would enable the interconnection of these devices (with different gas sensors) to generate a complete mapping of an urban area. Electronic noses have emerged as a low-cost, portable tool capable of detecting and quantifying these pollutants in real time, providing valuable information for implementing preventive and corrective measures [14].

In this work, we present gas sensors made with SnO_2 and ZnO and manufactured using different fabrication methods for the detection of these pollutant gases (NO_2 and CO), with key figures of merit, such as sensitivity, linear measurable range, the root mean squared deviation (RMSnoise), the limit of detection (LOD), and responses/recovery times extracted and compared.

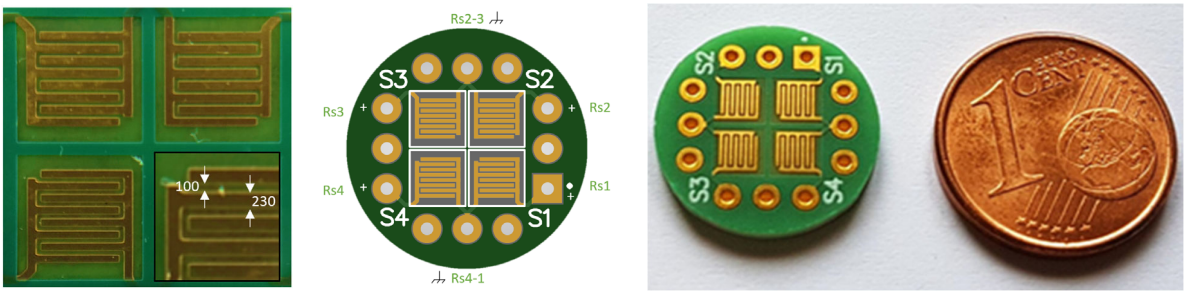
2. Materials and Methods

2.1. Substrate

In this work, the aim is to compare gas sensors fabricated with the same materials but using different preparation methods. Although the same materials were used, the preparation processes differ, as each method requires the precursor material to be in a different form, or the dispersion used must be prepared differently, depending on the specific method required for generating the sensing layer on the sensor.

In all cases, these sensing layers were deposited on FR-4 substrates, manufactured by Eurocircuits NV (Mechelen, Belgium). FR-4 is an epoxy-reinforced glass laminate material used for printed circuit boards due to its flame resistance and near-zero water absorption. On the surface of the substrate, interdigitated electrodes (IDTs) are arranged to measure the resistance of the sensors which, along with the sensor contacts, are made of copper.

The IDTs consist of four pairs of fingers with a width of 0.23 mm and a spacing of 0.1 mm between fingers, resulting in an active sensor area of 2.87 × 2.87 mm^2. As shown in Figure 1, the substrate consists of four membranes on which the NPs can be deposited.



(**a**) (**b**) (**c**)

Figure 1. Multisensor platform: (**a**) Substrate layer detail; (**b**) Sensor electrode configuration; (**c**) Scale of the substrate.

The sensors were prepared using SnO_2 and ZnO nanoparticles with each of the fabrication methods.

2.1.1. Drop-Casting

For the preparation of the different sensing layers, an automatic "dropcaster" device was used. This equipment is custom-designed and built in-house, and its characteristics are described in previous works [15,16]. The equipment allows for precise control of process parameters such as droplet size, deposition time, wait time between droplets, and deposition volume.

SnO_2 NPs (<100 nm in size) and ZnO NPs (<50 nm in size) were used along with deionized (DI) water, all acquired from Sigma Aldrich (Burlington, MA, USA). Initially, dispersions of SnO_2 and ZnO NPs in DI water were prepared by sonication at a concentration of 2.5 mg mL^{-1}. The sensing layers were obtained by depositing the different dispersions through drop-casting onto the multisensor platform. During the process, a droplet size of 150 nL and a wait time of 150 s between droplets were used to ensure complete evaporation of the solvent in each deposited droplet. A total volume of 210 µL of each material was deposited.

During the deposition, the substrate was illuminated with a set of infrared LEDs to promote solvent evaporation. DI water was used for these dispersions because it has the necessary surface tension to make the droplets more compact and remain within the active area, despite being less volatile than other solvents.

2.1.2. Electrospray

To prepare the sensing layers using electrospray, the commercial Spinbox equipment from Fluidnatek (Valencia, Spain) was used. This device allows for the fabrication of sensing films from different dispersions using this technique and provides control over various deposition parameters. It is equipped with a micropump that supplies the necessary flow rate for the process. The electrospray process is carried out inside the equipment, where the support holding the needle is located. The needle is connected to the micropump, and a plate is provided for placing the multisensor array for material deposition. This equipment allows control over the potential difference between the emitter and receiver plates, as well as the distance between them. It also includes a camera for monitoring the process. Finally, all systems are controlled by a PC. Figure 2 shows this equipment.

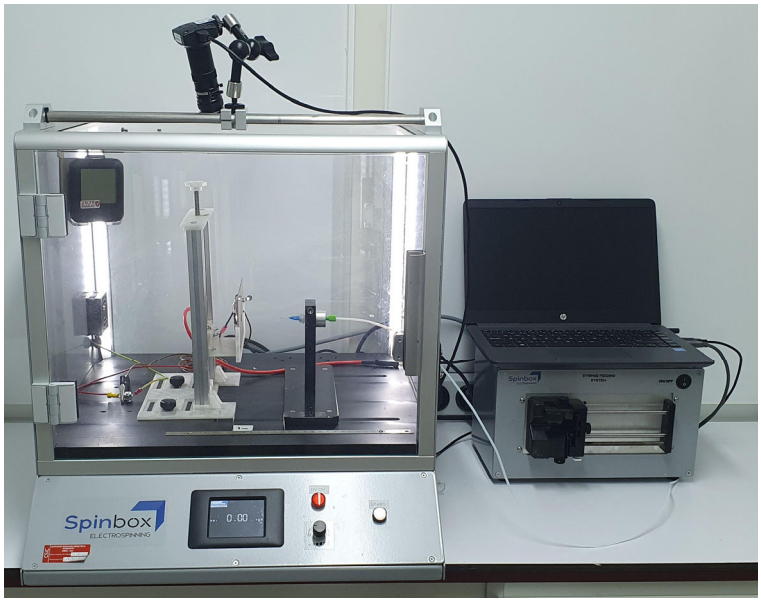


Figure 2. Spinbox electrospray equipment.

The same materials described in the previous section were used. In this case, the dispersions with SnO_2 and ZnO NPs were prepared in ethanol from Sigma Aldrich, at a concentration of 2.5 mg mL^{-1}. Ethanol was chosen because this sensor fabrication technique requires a solvent with higher volatility.

Once the dispersions were prepared, the SnO_2 and ZnO films were deposited. During the process, a potential difference of 4.6 kV was applied, with a needle-to-substrate distance of 2 cm, a flow rate of 2.5 µL min^{-1}, and a duration of 30 min. The deposition was carried out under conditions of 27.5 °C and 30% relative humidity (RH). A flat-head Ga. 22 needle was used.

2.1.3. Spark Ablation Coupled with a Programmable Dry Printing System

Spark ablation technology is an attractive scalable aerosol route for NP generation. Nanostructured materials with a high degree of purity are obtained, as no solvents or chemical ligands are involved during the synthesis. These properties make spark ablation a nanotechnological material production technique based on sustainable principles [17]. This purely physical process occurs at an ambient pressure and room temperature, only requiring electricity, a carrier gas, and electrode material to produce NPs. Figure 3 shows a schematic representation of the working principle of the NP generation based on the spark ablation technique. In short, material ablation results from a high-tension electrical spark applied between two opposing electrodes, leading to the formation of vaporized material in the vicinity of the spark zone due to the locally high temperatures achieved [18]. The introduction of a carrier gas causes rapid condensation, creating atomic clusters that evolve to form primary NPs and subsequently agglomerates of NPs. A wide variety of NPs can be produced using this technique, as it can be applied to any metallic, metallic alloy, or properly doped semiconductive material.

The aerosol containing NPs produced can be collected and subsequently deposited onto a target substrate through different methods such as electrostatic precipitation, filtration [17], or impaction [19]. For gas sensing applications, the impaction method appears to be the most suitable when the sensing layer material needs to be deposited in a pre-defined area [20]. This deposition method relies on accelerating an aerosol through a nozzle toward a chamber at lower pressure, where the target substrate is located. As a result, the aerosol is

accelerated to supersonic speeds and impacts the target substrate. By coupling the process to substrate XYZ stage, arbitrary patterns can be printed in a single-step process.

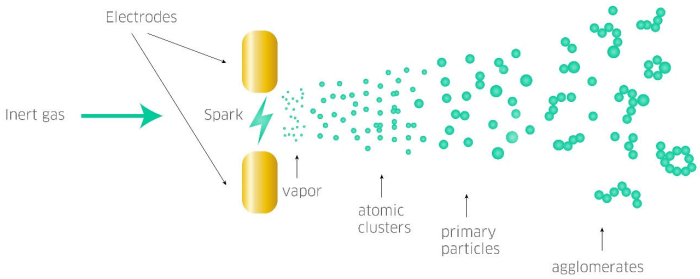


Figure 3. Operating principle of the VSP-G1.

In the present work, the spark ablation generator VSP-G1 (VSParticle B.V., Delft, The Netherlands) was used to produce nanoparticulate material. Sn and Zn electrodes with a diameter of 6 mm and a purity of 99.99% were used for the spark ablation process. Argon was employed as the carrier gas, with a constant flow rate of 1 L min^{-1}. Table 1 includes the sparking potential for the generation and subsequent deposition of each sensing material. A Nanoprinter tool (VSP-P1, VSParticle B.V.), based on the impaction principle, was used to print the sensing layer onto the IDE structures. The system operated at 0.2 mbar, with a nozzle featuring a circular orifice of 100 µm diameter and resulting throughput of 0.08 L min^{-1}. The nozzle-to-substrate distance was maintained at 500 µm. For the deposition of base materials such as SnO_2 and ZnO, a 500 nm thick continuous nanoporous layer (NPL) was printed. Table 1 indicates the printing speed and number of passes (number of overprints) for each printed material. To cover the entire IDE with the NPL, a script was executed following a vertical serpentine pattern.

Table 1. Summary of spark ablation power and printing parameters.

Electrode	Potential [kV]	Current [mA]	Printing Speed [mm s^{-1}]	Number of Passes
Sn	1.3	10	0.2	4
Zn	1.3	10	0.2	2

2.2. Experimental Setup

The sensing properties of the sensors were evaluated using an automated multichannel testing system. The fabricated sensor array was optically and electrically characterized simultaneously when exposed to atmospheres with different concentrations of atmospheric pollutants. For this purpose, the setup shown in Figure 4 was used, which was controlled by a PC using custom software developed in LabVIEW (2024 Q1). The setup can be divided into three parts:

- Gas Mixing: To obtain the target gas mixtures, calibrated gas cylinders of NO_2 and CO (certified by Nippon Gases S.L.U.) were used. The reference gases were diluted using synthetic air (certified by Nippon Gases S.L.U.) by adjusting the respective flow rates through a gas mixing unit from IRay (Cáceres, Spain), maintaining a constant total flow of 100 mL min^{-1}. This equipment allows the generation of mixtures with different humidity levels. The resulting gas mixture is passed through a stainless-steel cell, where the multisensor array is located.
- Electrical Characterization: This was carried out using a Keithley 6517 electrometer (Cleveland, OH, USA) at a constant bias voltage of 15 V.
- Optical Characterization: The sensor surface was illuminated with a UV LED (model LSM-365A Light Source) with a wavelength of 365 nm, controlled by the LDC-1 single-channel LED controller. The LED has a full width at half maximum (FWHM) of 12 nm

and a nominal wavelength of 365 nm, meaning it emits light in the range of 359 nm to 371 nm. Additionally, a discrete band-pass filter is connected to the LED output to eliminate any contribution above 380 nm due to reflection or refraction effects of the light itself. This source allows the emission of different types of signals, as well as power modulation. The LED is connected to the cell at a 45° angle relative to the sensor surface, and the generated photoluminescence is collected at a 90° angle using the HR2 UV-VIS spectrometer. All equipment used for the optical characterization of the sensors was provided by Ocean Insight (Largo, FL, USA).

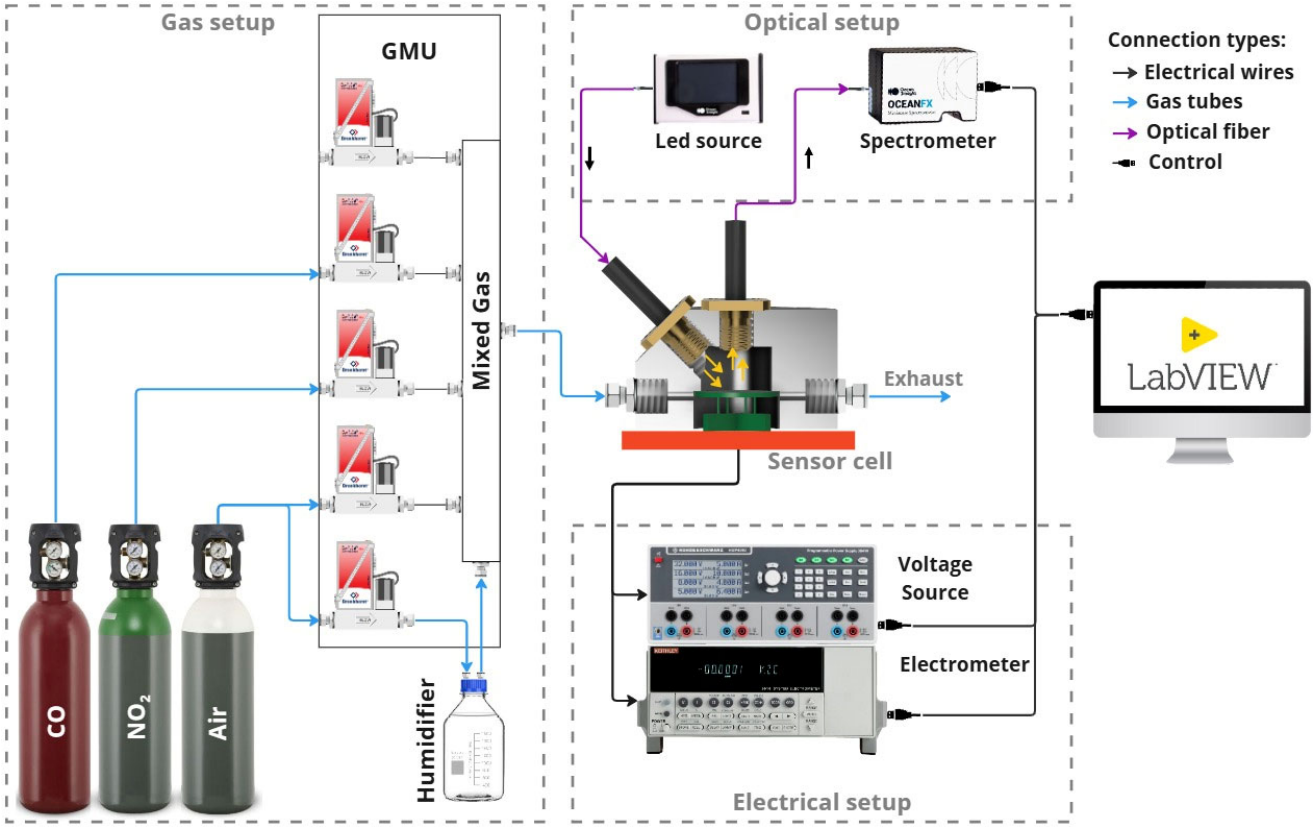


Figure 4. Measurement setup for laboratory experiments.

Each measurement is divided into two phases: desorption and adsorption. The first phase lasted 30 min, and the second phase lasted 15 min. The cycle durations could be reduced, but according to the research group's protocol, these times were initially used and can be optimized as the project progresses. The response of the sensors to the reference gases was estimated by the change in resistance, as follows:

$$\text{Response } (\%) = (R_a - R_g/R_g) \times 100, \quad (1)$$

$$\text{Response } (\%) = (R_g - R_a/R_a) \times 100, \quad (2)$$

where R_a is the initial resistance of the sensor in air atmosphere and R_g is the resistance measured after being exposed to test gas. Equation (1) is used for reducing gases, while Equation (2) is used for oxidizing gases.

3. Results

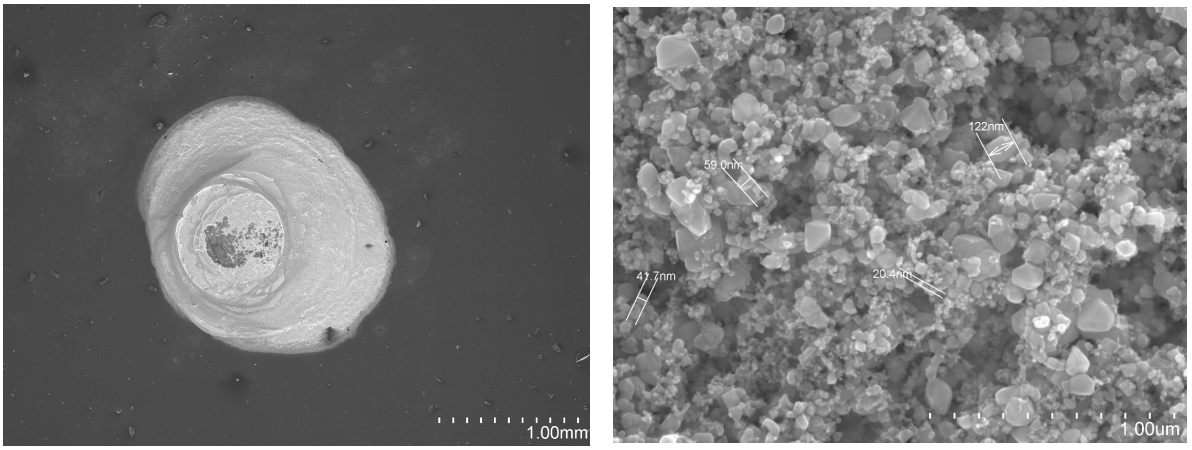
3.1. Sensitive Layer Characterization

For the characterization of the sensing films, two SEM tools were used. On one hand, the samples fabricated by drop-casting and electrospray were characterized at the University of Extremadura (UEx). The Quanta 3D FEG (FEI Company, Hillsboro, OR, USA) was used to study the morphology and composition of the sensing layer. On the other hand, the samples fabricated by spark ablation were characterized at TU Delft using ultra-high-resolution FE-SEM model Regulus 8230 (Hitachi High-Tech, Tokyo, Japan). Additionally, these latter samples were characterized by XPS at the UEx, using FlexPS-ARPES-E equipment (SPECS Group, Berlin, Germany). All sensing layers were prepared under the same conditions as the sensors, using the same materials but deposited on silicon substrates.

3.1.1. Characterization of Drop-Casting Samples

SEM images of the sensing layers deposited by drop-casting show a very similar surface morphology across all depositions. Aggregates of nanoparticles and randomly distributed mesopores can be observed.

In Figure 5a, the distribution of SnO_2 NPs can be seen at a lower magnification. Areas with a higher concentration of material and others, in the center, with thinner layers can be observed, reflecting the heterogeneity inherent to this deposition technique.

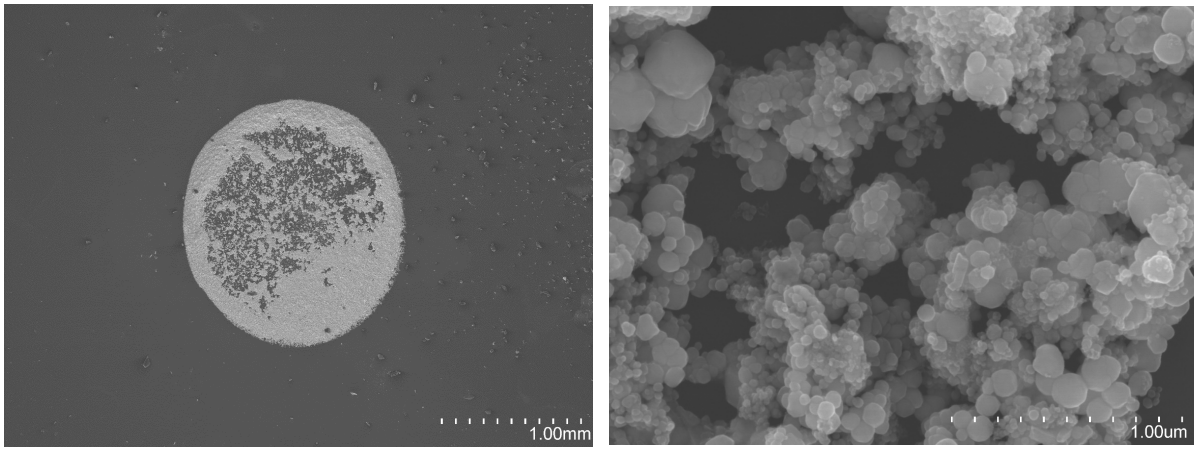


(**a**) (**b**)

Figure 5. SEM images of a SnO_2 sensitive layer fabricated by drop-casting: (**a**) Overview image showing the morphology of the layer at the millimeter scale; (**b**) Detailed image revealing the nanoscale features of the layer.

The NPs are quasi-spherical in shape, with sizes below 100 nm. Asymmetrical aggregates of NPs with different geometries (rectangular or radial) and sizes greater than 100 nm can also be observed (Figure 5b). The formation of these aggregates is due, on one hand, to the large surface area of the NPs, which promotes their affinity for each other. On the other hand, it is also a result of the sample preparation process, in which the NPs overlap one another.

In the case of the ZnO sample fabrication, it can be observed at a lower magnification that there is a more homogeneous layer in the outer ring, while the central area has a lower density of NPs (Figure 6a). In Figure 6b, greater porosity and even areas without material can be observed. As seen in the previous case, a random distribution of quasi-spherical NPs of different sizes and aggregates of larger NPs can be observed, with some even reaching sizes greater than 200 nm.



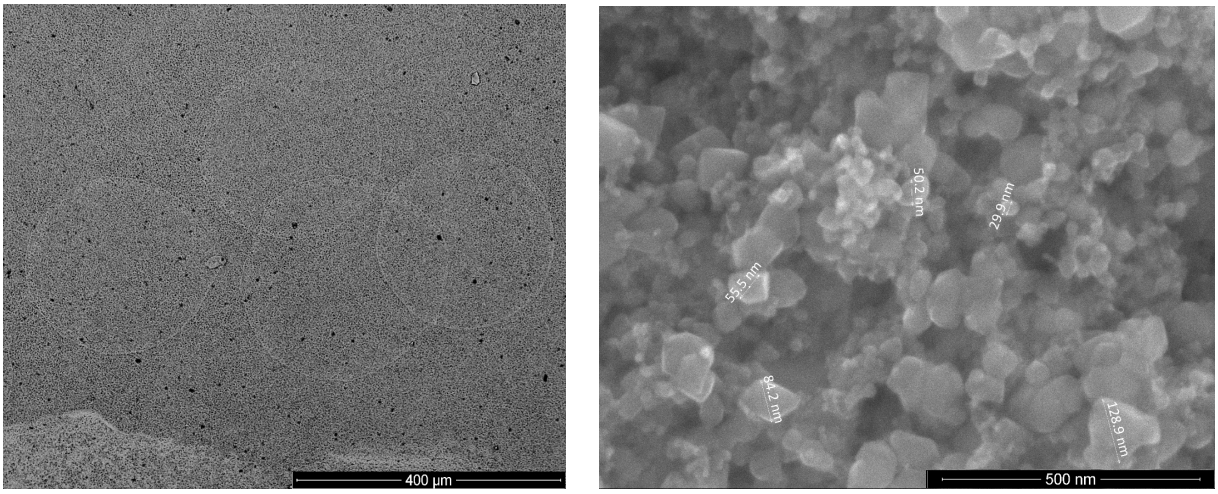
(**a**) (**b**)

Figure 6. SEM images of a ZnO sensitive layer fabricated by drop-casting: (a) Overview image showing the morphology of the layer at the millimeter scale; (b) Detailed image revealing the nanoscale features of the layer.

The thickness and roughness of the deposited layers were measured using a Veeco Dektak 6M profilometer (Plainview, NY, USA). The central region exhibited an average thickness of approximately 1.5 µm. Figure S1 presents a representative curve obtained for the ZnO film. Additionally, the sample's average roughness was measured, yielding values around 350 nm.

3.1.2. Characterization of Electrospray Samples

The SnO_2 samples produced by electrospray show greater homogeneity in the deposited material layer at a lower magnification (Figure 7a). Circular shapes can also be observed, which were deposited during the electrospray process due to the formation of larger droplets. This can occur if, during the electrospray process, the regime temporarily shifts to a non-stationary state.

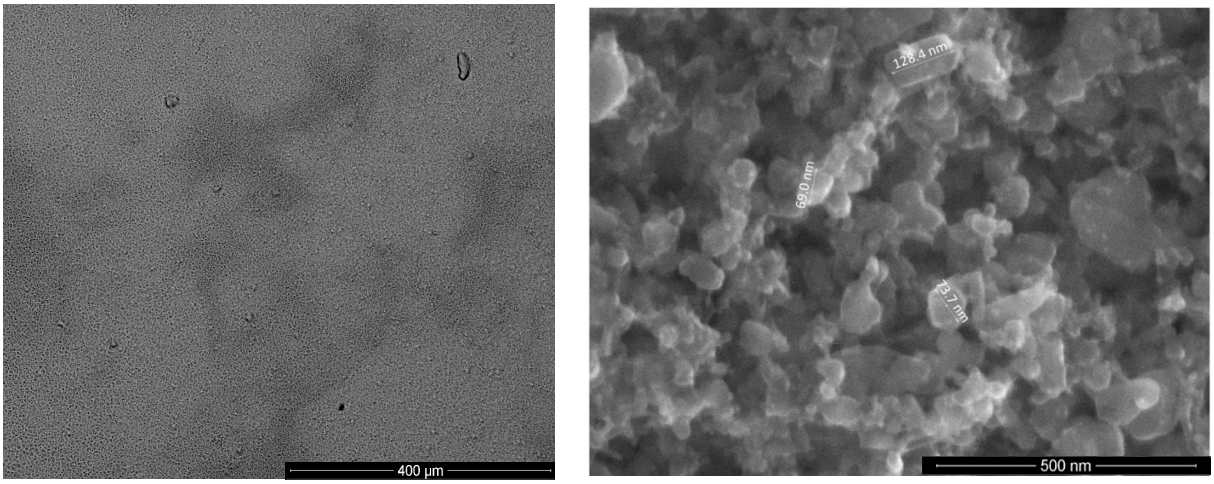


(**a**) (**b**)

Figure 7. SEM images of a SnO_2 sensitive layer fabricated by electrospray: (**a**) image at 350× magnification and (**b**) image obtained at 250,000× magnification.

On the other hand, in Figure 7b, NPs of different sizes, smaller than 100 nm, can be observed, with some being significantly smaller. Additionally, some aggregates slightly larger than 100 nm are visible. High porosity of the deposited material is also observed.

The ZnO sensing layer, as shown in Figure 8a, is homogeneous except for a few isolated aggregates. Small NPs and aggregates ranging between 50 and 150 nm can be observed (Figure 8b). The porosity of the material produced during the deposition process is also evident.



(**a**) (**b**)

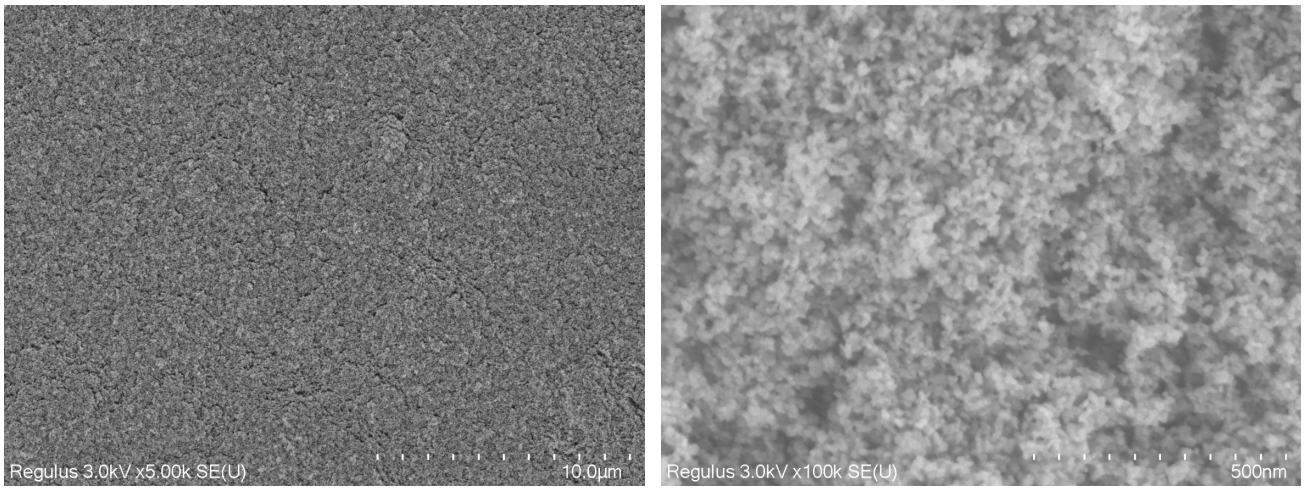
Figure 8. SEM images of a ZnO sensitive layer fabricated by electrospray: (**a**) image at 350× magnification; (**b**) image obtained at 250,000× magnification.

In this case, the thickness of the deposited film was measured in the same way as for the samples manufactured by drop-casting, whose curve is shown in Figure S1. The average thickness is 1 µm, and the average roughness of the sample is 93.6 nm.

3.1.3. Characterization of Spark Ablation Coupled with a Programmable Dry Printing System Samples

For this technique, Figure 9 shows an example of the homogeneous distribution exhibited by the samples prepared using this method. The size of the NPs is much smaller than in the previous methods, and no clusters are observed. Therefore, SEM analysis is suitable for assessing the uniformity of the nanoporous layers (NPLs) but not for determining the NP size due to their relatively small dimensions. TEM measurements revealed NP sizes on the order of 20 nm, as shown in Figure S2 in the Supplementary Materials.

With this method, the thickness of the deposited layer can also be controlled with much greater precision compared to the other two methods. Since the method used allows the fabrication of sensors with SnO_2 and ZnO with the same characteristics, only one sensor made with the latter material has been shown as an example. Figure S3 shows an SEM image of a SnO_2 sensing layer deposited by spark ablation. To measure the thickness of the printed lines, 2 mm long lines were printed on a Si-based substrate using identical parameters to those used for the prints on the sensor platform. Subsequently, the Si substrate was cleaved at the central part of the printed line. Cross-sectional SEM was performed to measure the thickness of the nanoporous layer. Figure S4 shows an SEM cross-sectional image of a ZnO nanoporous layer. A calibration curve of the measured nanoporous layers, depending on the number of passes, was generated. For device fabrication, the printing conditions shown in Table 2 were adopted to target an average layer thickness in the central part of the line of 450 ± 10 nm.



(**a**) (**b**)

Figure 9. SEM images of a ZnO sensitive layer fabricated by spark ablation: (**a**) Overview image showing the morphology of the layer at the micrometer scale; (**b**) Detailed image revealing the nanoscale features of the layer.

Table 2. Stoichiometric quantification of samples deposited by spark ablation for each fabricated sensor.

Quantification Results	SnO_2	ZnO
O1s	49.12%	35.67%
Sn3d	25.00%	—
$Zn2p_{3/2}$	—	36.62%

Since it is a physical deposition method, XPS characterization was performed on the samples generated by spark ablation to analyze the composition of the deposited layer. It was found that, in the SnO_2 sensors, oxygen was present in a stoichiometric ratio of twice that of tin. In contrast, in the ZnO sensors, the ratio of oxygen to zinc was practically 1:1. In this study, the sensing layers were oxidized upon exposure to the ambient environment after unloading the samples from the Nanoprinter. Alternatively, oxygen gas can be introduced into the carrier gas to promote the formation of oxidized particles during NP generation [17], or annealing in an oxygen-rich atmosphere can be performed [21].

3.2. Electrical Characterization

The electrical characterization of the sensors fabricated using the three different techniques was carried out using the gas line described in Section 2.2. The results obtained for each case are presented below, showing the responses of the sensors when exposed to the two target gases (NO_2 and CO). The measured concentrations for each gas are listed in Table 3. All measurements were performed at 50% relative humidity.

Table 3. Measured concentrations of the target gases.

Gases	Bottle Concentration	Measured Concentrations
NO_2	1.14 ppm	100, 200, 300, 400 and 500 ppb
CO	10 ppm	1, 2, 3, 4 and 5 ppm

3.2.1. NO_2 Sensing Performance

All sensors fabricated by drop-casting, electrospray, and spark ablation exhibited a response to NO_2, with varying degrees of sensitivity (Figure 10). In general, SnO_2 sensors outperformed ZnO sensors at low concentrations. However, at high concentrations, the

ZnO sensor fabricated by spark ablation achieved the highest response, reaching 79% at 500 ppb, whereas the other sensors only reached 50% or 35%.

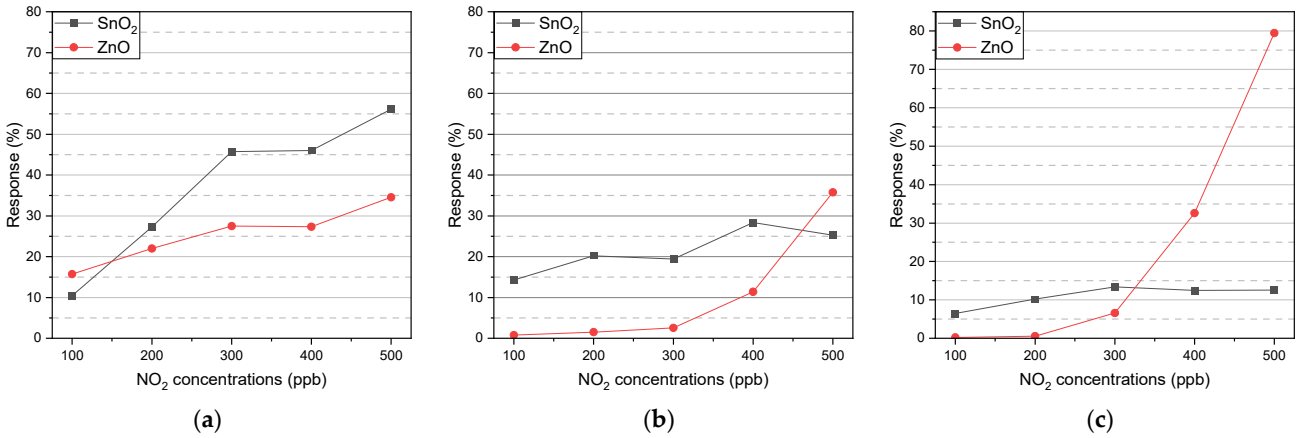


Figure 10. NO_2 sensing response of sensors fabricated by different techniques: (**a**) drop-casting; (**b**) electrospray; (**c**) spark ablation.

At very low concentrations, all sensors were able to detect NO_2, with the SnO_2 sensor fabricated by electrospray exhibiting a 15% response at 100 ppb. Among the different fabrication techniques, drop-casting resulted in the highest response variation between 100 and 300 ppb (35%), but remained almost constant beyond 300 ppb. For sensors fabricated by electrospray, the SnO_2 sensor exhibited a greater response at lower concentrations, though with less variation across the tested range. Similarly, for sensors fabricated by spark ablation, the SnO_2 sensor exhibited a higher response at low concentrations, while ZnO sensors fabricated by this method showed a significantly stronger response at 500 ppb.

3.2.2. CO Sensing Performance

The SnO_2 sensors fabricated using the three techniques exhibited a significantly stronger response to CO compared to the ZnO sensors, which showed minimal or no detection capability. Figure 11 shows the responses of all sensors in the presence of CO at different concentrations.

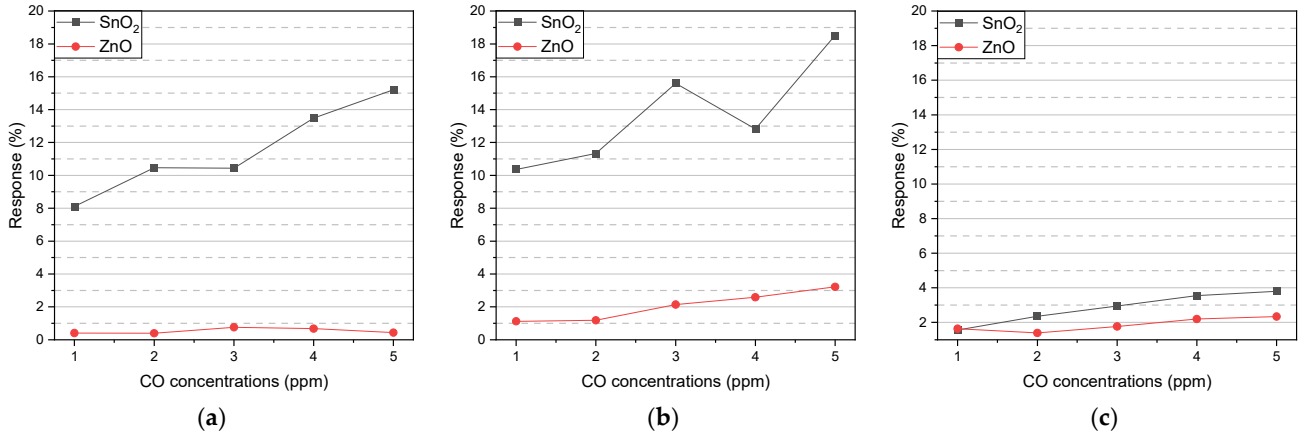


Figure 11. CO sensing response of sensors fabricated by different techniques: (**a**) drop-casting; (**b**) electrospray; (**c**) spark ablation.

At room temperature, all SnO_2 sensors were able to detect CO at low concentrations. Those fabricated by electrospray and drop-casting exhibited the highest responses, reaching 18% at 5 ppm and 10% at 1 ppm for electrospray-fabricated sensors, while the responses of

drop-cast sensors were slightly lower. The response variation for drop-cast SnO_2 sensors between 1 and 5 ppm was approximately 7.5%, with a maximum response of 15% at 5 ppm.

Regarding ZnO sensors, their response to CO was considerably weaker. The ZnO sensor fabricated by drop-casting did not differentiate between concentrations, showing no clear trend. In contrast, the ZnO sensor obtained by electrospray, despite its low response, was still able to detect CO. Sensors fabricated by spark ablation exhibited the lowest responses for both SnO_2 and ZnO, but they were still capable of detecting CO, with slight variations between different concentrations.

In the Supplementary Materials, Figure S5 shows, as an example, the dynamic response of a sensor fabricated by spark ablation in the presence of NO_2 and another fabricated by electrospray in the presence of CO. Both sensors exhibit n-type behavior and demonstrate good recovery after each measured concentration.

3.3. Optical Characterization

As indicated in Section 2.2, electrical and optical characterization was carried out simultaneously. Figure 12 shows the spectra obtained with the ZnO sensor in the presence of air (during the cleaning or desorption phase) and the spectrum in the presence of 500 ppb of NO_2 (during the adsorption phase).

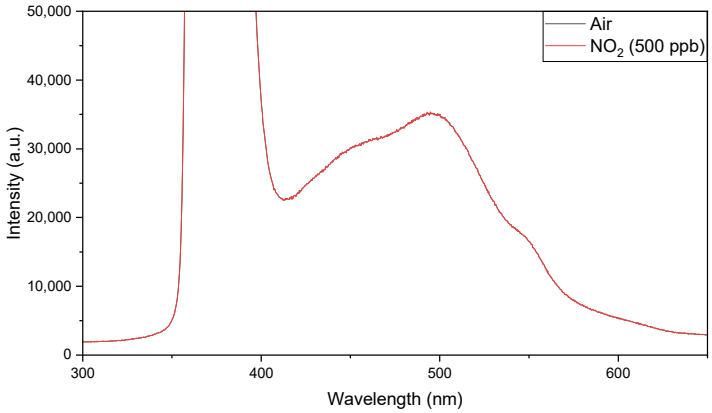


Figure 12. Optical response of the ZnO sensor fabricated by spark ablation.

Two peaks can be observed: the first one, which is saturated, corresponds to the wavelength of the LED (365 nm). Additionally, there are two relative maxima centered at 500 nm and 550 nm, attributed to the intrinsic photoluminescence of the metal oxide. Figure 12 shows no spectral differences when the sensor was exposed to an atmosphere containing NO_2 compared to air. Similarly, no differences were found for the other sensors, regardless of the fabrication method used; therefore, their spectra are not included.

Notably, the UV LED played a crucial role in facilitating sensor cleaning during the desorption phases interspersed between each measurement or adsorption phase.

4. Discussion

Once the responses of the sensors for each fabrication method have been described, we proceed to compare them to determine the advantages and disadvantages observed in each case.

It was observed that the baseline resistance of sensors fabricated by electrospray was lower than that of sensors produced by spark ablation and drop-casting. Specifically, electrospray-fabricated sensors exhibited resistances in the MΩ to GΩ range, whereas the other two techniques yielded resistances at least one order of magnitude higher. However, it is worth noting that the geometry of the printing layers was different in each technique.

It is expected that if thicker layers are produced by the spark ablation technique, the device resistance will decrease. Resistivity measurements are the most suitable metric to define the electrical transport properties and the baseline of the sensor device, since resistivity is a material property independent of geometry and thickness. This allows the normalization of resistance differences caused by variations in the sensing film. Table S1 shows the calculated resistivity values. These values were obtained from the average baseline resistance of each sensor, using a simplified geometrical approximation based on the dimensions of the interdigitated electrodes (electrode length and gap width between IDTs), and the measured thickness of the sensing layer for each deposition technique [22].

To further analyze their electrical behavior, V-I curves were recorded (Figure S6). These curves indicate that all sensors exhibit ohmic behavior for both ZnO and SnO_2, meaning their resistance remains constant over the applied voltage range. However, the SnO_2 sensor fabricated by drop-casting shows a slight deviation at intermediate voltages, possibly due to a less homogeneous distribution of the deposited layer. Despite this deviation, the overall trend remains linear.

This difference is significant, as the goal of developing these sensors is to integrate them into portable, cost-effective devices capable of deployment in diverse locations for extensive field measurements under real-world conditions. Unlike electrometers, which can measure a broad range of resistances, these portable devices have more limited measurement capabilities. In this regard, sensors fabricated by electrospray offer a distinct advantage.

Tables 4 and 5 summarize key performance metrics derived from the resistance variations upon exposure to target gas molecules, including RMS noise, measurable range, and response/recovery times, as well as the calibration curve parameters (sensitivity, linearity, and LOD). For the RMS noise calculation, the procedure implemented in [23] was adopted in this work. Response and recovery times were defined as the time required to reach 90% of the final response and to recover 90% of the baseline resistance, respectively.

Table 4. Sensors metrics for NO_2. Sensitivity (S) is defined as the slope of a linear fit obtained from the calibration curve (R vs. C), where R represents the response and C the concentration. RMS refers to the root mean squared. ND indicates that the value is not defined within the analyzed range.

Material Generation Technique	Sensing Material	Measurable Range [ppm]	Linear Range [ppm]	S [%/ppm]	R-Squared Coefficient	RMS Noise [ppm^{-1}]	LOD [ppm]	Response Time-R_{90} @ 0.3 ppm [Min]	Recovery Time-R_{10} @ 0.3 ppm [Min]
Electrospray	ZnO	ND	-	-	-	0.13	-	4.5	10.25
	SnO_2	ND	-	-	-	0.42	-	1.5	4.5
Drop-casting	ZnO	0.1–0.5	0.1–0.3	63.3 ± 0.2	0.97	0.22	0.01	3.25	4.75
	SnO_2	ND	0.1–0.3	130 ± 14	0.999	0.7	0.017	2.25	4.75
Spark Ablation	ZnO	0.1–0.5	0.3–0.5	214 ± 28	0.96	0.05	-	13.25	3
	SnO_2	0.1–0.5	0.1–0.3	370 ± 25	0.99	0.005	0.0055	4.75	3

In general, all sensing layers produced using the spark ablation technique generate low-noise signals, quantified by the RMS noise value, which is derived from the device baselines. Specifically, SnO_2 nanoporous layers exhibit the lowest RMS noise values, ranging from 0.005 to 0.02 ppm^{-1}. This represents a significant advantage in data processing, as it eliminates the need for additional filtering steps. Furthermore, baseline stability is crucial for achieving low LOD values.

Table 5. Sensors metrics for CO.

Material Generation Technique	Sensing Material	Measurable Range [ppm]	Linear Range [ppm]	S [%/ppm]	R-Squared Coefficient	RMS Noise [ppm^{-1}]	LOD [ppm]	Response Time-R_{90} @ 3 ppm [Min]	Recovery Time-R_{10} @ 3 ppm [Min]
Electrospray	ZnO	1–5	1–5	1 ± 0.2	0.83	0.11	0.4	12	6
	SnO_2	ND	-	-	-	0.75	-	11	9.75
Drop-casting	ZnO	ND	-	-		0.18	-	-	-
	SnO_2	ND	-	-		1.22	-	-	-
Spark Ablation	ZnO	1–5	1–5	0.29 ± 0.04	0.9	0.036	0.61	6.75	7.5
	SnO_2	1–5	1–5	0.69 ± 0.05	0.97	0.02	0.1	9.75	10

A broad linear response (or linearity in an alternative scale such as log-log) is a highly desirable property in gas sensors [24]. Sensing layers fabricated by spark ablation exhibit a higher R-squared coefficient within a defined linear range compared to those produced by electrospray and drop-casting. Additionally, a consistent linear range was observed across all analyzed gas concentrations for sensing layers produced by spark ablation. In terms of response time, all tested devices exhibited characteristic response and recovery times within a range of a few minutes. The fastest response times for CO detection at 3 ppm were achieved with SnO_2 devices fabricated by electrospray.

Sensors fabricated by spark ablation exhibited superior responses to NO_2 at the highest concentration (500 ppb), except for the SnO_2 sensor. For the other three sensors, the measurement trends were similar. ZnO sensors demonstrated higher responses than SnO_2 sensors, except for the SnO_2 sensor fabricated by drop-casting.

The drop-casting and electrospray sensors exhibited better responses in the presence of CO, except for the ZnO sensor, which had a response very similar to that of the electrospray-fabricated sensor. The SnO_2 sensors performed better in terms of responses compared to the ZnO sensors. In the presence of this gas, the responses were lower compared to NO_2, and generally, a smaller difference in response was observed between lower and higher concentrations. Conversely, SnO_2 sensors fabricated by spark ablation and ZnO sensors produced by electrospray exhibited the highest responses to CO.

Figure 13 presents a radar chart to facilitate the comparison of the different sensors in terms of the evaluated parameters. To simplify this comparison, the average values for each parameter from Tables 4 and 5 were calculated separately for NO_2 and CO. The average R-squared coefficient values were normalized, while the values of RMS noise, LOD, response time, and recovery time were inversely normalized. This ensures that higher values always indicate better performance. The sensitivity metric was excluded, as sensor response differences were more clearly analyzed throughout the study.

As previously mentioned, the sensors exhibited better performance in the presence of NO_2 than in the presence of CO. For this reason, the data were split into two charts to allow more specific conclusions. In general, and corroborating previous observations, the sensors fabricated by spark ablation achieved higher ratings in terms of the R-squared coefficient, RMS noise, and LOD. However, their response and recovery times were not the fastest, particularly in the NO_2 measurements. Despite this, these sensors exhibited higher repeatability in the parameters of different sensors, as the recovery-related metrics were relatively homogeneous in both graphs, except for the LOD value.

In contrast, the sensors fabricated using the other two techniques showed greater variability in the metrics among sensors manufactured with the same technique. The drop-casting sensors performed well for NO_2 detection, particularly excelling in response and recovery times. However, they performed poorly in the presence of CO, preventing the establishment of a linear response, whether on a linear or log-log scale. Similarly, electrospray-fabricated sensors showed comparable response and recovery times to those

of the spark ablation sensors, but they performed better in the presence of CO than in the presence of NO_2, contrary to the trend observed in drop-casting sensors.

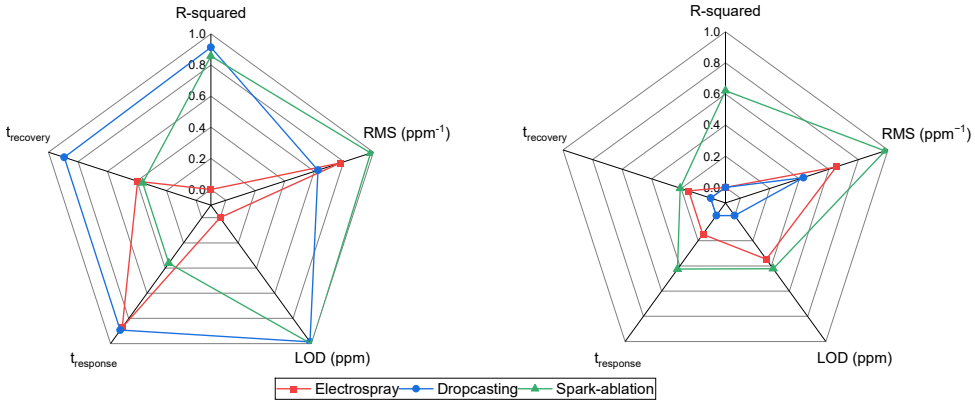


Figure 13. Comparison of metrics for the three fabrication techniques, showing the normalized average values of all sensors manufactured by each technique, separately for each gas measured: (**a**) NO_2 and (**b**) CO.

It is important to highlight that the presented devices were not fully optimized for the detection of specific target gas molecules (i.e., the deposition parameters such as nanoparticle sizes and layer thickness could be further refined). However, the collected results provide sufficient evidence to evaluate the simplicity and control of the sensing layer fabrication process, as well as key sensor performance metrics that do not necessarily depend on material optimization to maximize response and sensitivity.

The detection efficiency of the sensing layers depends on the available surface area for interactions with surrounding gases; therefore, their detection performance is closely related to their surface characteristics (i.e., grain size, shape, and surface porosity). Nanomaterials, such as the nanoparticles used in this study, provide a high surface-to-volume ratio and facilitate gas diffusion [25,26].

Regarding surface morphology, the sensors prepared by drop-casting and electrospray exhibited very similar structures, with randomly distributed nanoparticles (<100 nm), agglomerates, and mesopores (2–50 nm). However, the drop-casting sensors contained more irregular nanoparticles and agglomerates, as well as larger pores (macropores >50 nm), as observed in the SEM images. In contrast, samples prepared by spark ablation did not form clusters, featured nanopores (<2 nm), and had smaller nanoparticles (~20 nm). Additionally, these sensors were significantly thinner (~450 nm) compared to those fabricated using the other two methods, which had thicknesses in the micron range.

Furthermore, the influence of sensing layer thickness on sensor performance needs to be carefully evaluated. Previous studies on conventional MOS-based devices printed by inertial impaction and fabricated by spark ablation have shown that thicker layers generally lead to higher response [20]. However, this aspect requires further investigation, particularly for room-temperature devices activated by UV illumination and for sensing layers operating at high temperatures (200–400 °C).

At low concentrations of target gases (NO_2 < 0.3 ppm and CO < 2 ppm), sensors fabricated by drop-casting and electrospray exhibited higher responses than those produced by spark ablation. This could be due to two primary factors—nanoparticle size and nanoparticle agglomerates, both of which can serve as active sites for gas interaction. Although the specific surface sites responsible for adsorption remain unclear, it is known that individual atoms or groups of atoms, adsorbed molecules, point defects, or surface dislocations can act as active sites [27].

Experimental data suggest that nanoparticle agglomeration acts as preferential adsorption points for the gas, enhancing the sensor response. As the gas concentration increases, these initially occupied points become unavailable, and the nanoparticles themselves begin to influence the sensor's response. Due to their high surface-to-volume ratio, nanoparticles exhibit high reactivity, with over 90% of their atoms exposed on the surface [27]. Consequently, smaller nanoparticles are advantageous for improving gas sensor sensitivity, as shown in Tables 4 and 5. Additionally, the thinner structure of sensors fabricated by spark ablation should, in principle, facilitate faster gas diffusion and detection. In general, the response and recovery times shown in Tables 4 and 5 confirm that this sensor exhibits shorter response times.

All sensors exhibit a higher response to NO_2 compared to CO, as NO_2 can interact with the semiconductor surface either by direct adsorption or through previously chemisorbed oxygen species [26,27], whereas CO interacts only with the oxygen species [27]. Finally, it should be noted that the sensors are capable of detecting CO concentrations as low as 1 ppm.

5. Conclusions

This study compares different fabrication methods of gas sensors using the same materials and substrate to assess the advantages and disadvantages of each method in detecting atmospheric pollutants. The thickness of the sensing layer varied across devices due to the limitations inherent to each fabrication method. Sensors composed of SnO_2 and ZnO were fabricated using drop-casting, electrospray, and spark ablation. The sensors produced with the first two techniques were produced in the NoySI group, while those manufactured by spark ablation were produced by the company VSParticle.

All sensors were capable of detecting the target gases (NO_2 and CO), but their performance varied significantly depending on the fabrication technique. Drop-casting is the simplest and most cost-effective technique, but it is the least reproducible. It offers less control over fabrication parameters, such as layer thickness and homogeneity. Sensors fabricated by drop-casting exhibited irregular nanoparticle agglomerates and larger pores (> 50 nm), which, while beneficial for gas diffusion at low concentrations, resulted in lower uniformity and higher baseline resistance (on the order of GΩ or higher). This technique showed better responses at low gas concentrations (NO_2 < 0.3 ppm and CO < 2 ppm), likely due to the presence of nanoparticle agglomerates acting as active adsorption sites. However, the lack of control over layer thickness and morphology limited its overall performance in terms of noise, linearity, and long-term stability.

Electrospray demonstrated better control over the deposition process compared to drop-casting, producing sensors with more uniform layers and smaller nanoparticle sizes (<100 nm). This technique resulted in lower baseline resistance values (with the implanted sensing layer geometries) than both drop-casting and spark ablation. It also exhibited good responses at low gas concentrations, particularly for CO detection, where SnO_2 sensors fabricated by electrospray showed the fastest response times at 3 ppm. However, this technique often led to nanoparticle agglomeration, which, while enhancing initial gas adsorption, reduced sensor performance at higher gas concentrations. Additionally, electrospray-fabricated sensors exhibited higher noise levels (RMS noise) compared to those produced by spark ablation, and their response linearity was less consistent.

Spark ablation emerged as the most promising technique, offering superior control over the fabrication process. The sensors produced using this method exhibited a smaller nanoparticle size (~20 nm), thinner layers (~450 nm), and a more uniform morphology with nanopores (<2 nm) and practically no agglomerates. These characteristics resulted in lower noise levels (RMS noise values ranging from 0.005 to 0.02 ppm^{-1}) and better

stability, making them suitable for portable devices. Additionally, spark ablation sensors demonstrated a wider linear response range and higher sensitivity. Furthermore, they showed fast response and recovery times, which are critical for real-time applications. However, their performance in terms of absolutes responses at low gas concentrations was slightly inferior to that of drop-casting and electrospray sensors.

In conclusion, beyond intrinsic performance, each fabrication technique has its own advantages and disadvantages that determine its suitability depending on the purpose and available resources. Drop-casting, due to its simplicity and low cost, is an excellent technique for the initial exploration of new materials or for quick proof-of-concept tests, requiring minimal investment in equipment and optimization time. Electrospray represents an intermediate option, offering better control and higher reproducibility than drop-casting. This makes it a good choice for more systematic and consistent studies at the laboratory scale, although it requires more time and financial investment. Finally, spark ablation allows the production of significantly more uniform and repeatable structures thanks to greater control over the deposition process. Although it is the most expensive and complex technique, it enables the fabrication of more robust sensors with higher performance, suitable for commercial applications or those requiring maximum reliability. Further studies are needed to fully understand the differences in detection mechanisms between sensors fabricated with each technique and to explore how morphology influences sensitivity and other relevant parameters. Additionally, optimizing the sensing layers will allow for a more comprehensive comparison of sensor performance under ideal conditions.

Supplementary Materials: The following supporting information can be downloaded at: https://www.mdpi.com/article/10.3390/chemosensors13060219/s1, Figure S1: Profilometry and rugosimetry of ZnO samples deposited by dropcasting (average roughness of 357.8 nm) and electrospray (average roughness of 93.6 nm); Figure S2: TEM images of the ZnO sensitive layer deposited by spark ablation; Figure S3: SEM images of a SnO_2 sensitive layer fabricated by spark ablation; Figure S4: SEM Cross-Section Images of Nanoporous Layers Deposited by Spark Ablation and Printed by Inertial Impaction on a Si Substrate: (a) SnO_2-based layer, (b) ZnO-based layer. The cross-section inspection was obtained printing a 2 mm long line and cleavage using a diamond pen to scratch a preferential direction that the Si follow after applying a force. The shown nanoporous layers has a mean thickness of (500 $\pm$ 30) nm. The thickness layer can be controlled by the number of repeatable overprints (at fixed spark ablation conditions). Printing at fixed spark ablation conditions and varying the number of passes is possible to extract a calibration curve to control the nanoporous layer thickness; Figure S5: Resistance variation: (a) sensor manufactured by spark ablation in the presence of NO_2, (b) sensor manufactured by electrospray in the presence of CO; Figure S6: V-I curves of the sensors fabricated with different techniques for each sensor material: (a) SnO_2, (b) ZnO; Table S1: Calculated baseline resistivity of the sensing layers as a function of manufacturing technique, composition, electrode dimensions and deposited thicknesses.

Author Contributions: Conceptualization, C.S.-V. and J.P.S.; methodology, C.S.-V., J.P.S. and I.S.; software, C.S.-V.; validation, C.S.-V., J.P.S. and I.S.; formal analysis, C.S.-V.; investigation, C.S.-V. and L.S.; resources, C.S.-V.; data curation, C.S.-V. and L.S.; writing—original draft preparation, C.S.-V.; writing—review and editing, C.S.-V., J.P.S., I.S., L.S. and V.M.; visualization, C.S.-V.; supervision, C.S.-V., J.P.S., I.S. and L.S.; project administration, J.P.S. All authors have read and agreed to the published version of the manuscript.

Funding: This work was supported by project TED2021-131114B-C22, financed by European Union NextGenerationEU/PRTR, and PID2023-151565OB-C42, funded by MICIU/AEI/10.13039/501100011033 and FEDER, UE.

Institutional Review Board Statement: Not applicable.

Informed Consent Statement: Not applicable.

Data Availability Statement: The original contributions presented in this study are included in the article. Further inquiries can be directed to the corresponding author.

Acknowledgments: SEM and XPS analysis was performed at the University of Extremadura.

Conflicts of Interest: Author Leandro Sacco was employed by the company VSParticle. Author Vincent Mazzola was employed by the company VSParticle. The remaining authors declare that the research was conducted in the absence of any commercial or financial relationships that could be construed as a potential conflict of interest.

References

1. European Environment Agency Air Pollution and Health—European Environment Agency. Available online: https://www.eea.europa.eu/publications/zero-pollution/health/air-pollution (accessed on 21 August 2024).
2. Beloconi, A.; Vounatsou, P. Revised EU and WHO Air Quality Thresholds: Where Does Europe Stand? *Atmos. Env.* **2023**, *314*, 120110. [CrossRef]
3. Potyrailo, R.A. Multivariable Sensors for Ubiquitous Monitoring of Gases in the Era of Internet of Things and Industrial Internet. *Chem. Rev.* **2016**, *116*, 11877–11923. [CrossRef] [PubMed]
4. Dennler, N.; Rastogi, S.; Fonollosa, J.; van Schaik, A.; Schmuker, M. Drift in a Popular Metal Oxide Sensor Dataset Reveals Limitations for Gas Classification Benchmarks. *Sens. Actuators B Chem.* **2022**, *361*, 131668. [CrossRef]
5. Berwal, P.; Sihag, S.; Rani, S.; Kumar, A.; Jatrana, A.; Singh, P.; Dahiya, R.; Kumar, A.; Dhillon, A.; Sanger, A.; et al. Hybrid Metal Oxide Nanocomposites for Gas-Sensing Applications: A Review. *Ind. Eng. Chem. Res.* **2023**, *62*, 14835–14852. [CrossRef]
6. Özgür, Ü.; Alivov, Y.I.; Liu, C.; Teke, A.; Reshchikov, M.A.; Doğan, S.; Avrutin, V.; Cho, S.J.; Morkoç, H.A. Comprehensive Review of ZnO Materials and Devices. *J. Appl. Phys.* **2005**, *98*, 041301. [CrossRef]
7. Krishna, K.G.; Parne, S.; Pothukanuri, N.; Kathirvelu, V.; Gandi, S.; Joshi, D. Nanostructured Metal Oxide Semiconductor-Based Gas Sensors: A Comprehensive Review. *Sens. Actuators A Phys.* **2022**, *341*, 113578. [CrossRef]
8. Zhang, C.; Luo, Y.; Xu, J.; Debliquy, M. Room Temperature Conductive Type Metal Oxide Semiconductor Gas Sensors for NO_2 Detection. *Sens. Actuators A Phys.* **2019**, *289*, 118–133. [CrossRef]
9. Wang, Z.; Bu, M.; Hu, N.; Zhao, L. An Overview on Room-Temperature Chemiresistor Gas Sensors Based on 2D Materials: Research Status and Challenge. *Compos. B Eng.* **2023**, *248*, 110378. [CrossRef]
10. Zhang, J.; Liu, X.; Neri, G.; Pinna, N. Nanostructured Materials for Room-Temperature Gas Sensors. *Adv. Mater.* **2016**, *28*, 795–831. [CrossRef]
11. Hyodo, T.; Urata, K.; Kamada, K.; Ueda, T.; Shimizu, Y. Semiconductor-Type SnO_2-Based NO_2 Sensors Operated at Room Temperature under UV-Light Irradiation. *Sens. Actuators B Chem.* **2017**, *253*, 630–640. [CrossRef]
12. Sayago, I.; Sánchez-Vicente, C.; Santos, J.P. Highly Sensitive and Selective SnO_2-Gr Sensor Photoactivated for Detection of Low NO_2 Concentrations at Room Temperature. *Nanomaterials* **2024**, *14*, 1994. [CrossRef] [PubMed]
13. Doyan, A.; Susilawati; Muliyadi, L.; Hakim, S.; Munandar, H.; Taufik, M. The Effect of Dopant Material to Optical Properties: Energy Band Gap Tin Oxide Thin Film. *J. Phys. Conf. Ser.* **2021**, *1816*, 012114. [CrossRef]
14. Gomes, J.B.A.; Rodrigues, J.J.P.C.; Rabêlo, R.A.L.; Kumar, N.; Kozlov, S. IoT-Enabled Gas Sensors: Technologies, Applications, and Opportunities. *J. Sens. Actuator Netw.* **2019**, *8*, 57. [CrossRef]
15. Sayago, I.; Santos, J.P.; Sánchez-Vicente, C. The Effect of Rare Earths on the Response of Photo UV-Activate ZnO Gas Sensors. *Sensors* **2022**, *22*, 8150. [CrossRef]
16. Santos, J.P.; Sanchez-Vicente, C.; Azabal, A.; Ruiz-Valdepenas, S.; Lozano, J.; Sayago, I.; Sanjurjo, J.L. Automation and Optimization Device for the Fabrication of Sensors with Nanomaterials. In Proceedings of the 2021 13th Spanish Conference on Electron Devices, CDE, Sevilla, Spain, 9–11 June 2021; pp. 129–131.
17. Ternero, P.; Sedrpooshan, M.; Wahlqvist, D.; Meuller, B.O.; Ek, M.; Hübner, J.M.; Westerström, R.; Messing, M.E. Effect of the Carrier Gas on the Structure and Composition of Co–Ni Bimetallic Nanoparticles Generated by Spark Ablation. *J. Aerosol Sci.* **2023**, *170*, 106146. [CrossRef]
18. Reinmann, R.; Akram, M. Temporal Investigation of a Fast Spark Discharge in Chemically Inert Gases. *J. Phys. D Appl. Phys.* **1997**, *30*, 1125. [CrossRef]
19. van Ginkel, H.J.; Mitterhuber, L.; van de Putte, M.W.; Huijben, M.; Vollebregt, S.; Zhang, G. Nanostructured Thermoelectric Films Synthesised by Spark Ablation and Their Oxidation Behaviour. *Nanomaterials* **2023**, *13*, 1778. [CrossRef]
20. Sacco, L.N.; Egger, L.; Popov, M.; Dösinger, C.; Romaner, L.; Schouten, N.; Köck, A. OT5.252 - Printing Nanoporous Layers (NPL) Generated by Spark Ablation for Gas Sensing Applications. *Lectures* **2024**, 141–142. [CrossRef]
21. Sacco, L.N.; Schouten, N.; Egger, L.; Popov, M.; Köck, A.; Dösinger, C.; Romaner, L. Multiarray Gas Sensors Based on Nanoporous Layers Produced à La Carte by Spark Ablation Using Metal Oxides, Binary and Ternary Alloys. In Proceedings of the IEEE Sensors, Kobe, Japan, 20–23 October 2024. [CrossRef]

22. Sharon, D.; Bennington, P.; Liu, C.; Kambe, Y.; Dong, B.X.; Burnett, V.F.; Dolejsi, M.; Grocke, G.; Patel, S.N.; Nealey, P.F. Interrogation of Electrochemical Properties of Polymer Electrolyte Thin Films with Interdigitated Electrodes. *J. Electrochem. Soc.* **2018**, *165*, H1028–H1039. [CrossRef]
23. Tang, H.; Li, Y.; Sokolovskij, R.; Sacco, L.; Zheng, H.; Ye, H.; Yu, H.; Fan, X.; Tian, H.; Ren, T.L.; et al. Ultra-High Sensitive NO_2 Gas Sensor Based on Tunable Polarity Transport in CVD-WS2/IGZO p-N Heterojunction. *ACS Appl. Mater. Interfaces* **2019**, *11*, 40850–40859. [CrossRef]
24. Potyrailo, R.A.; Go, S.; Sexton, D.; Li, X.; Alkadi, N.; Kolmakov, A.; Amm, B.; St-Pierre, R.; Scherer, B.; Nayeri, M.; et al. Extraordinary Performance of Semiconducting Metal Oxide Gas Sensors Using Dielectric Excitation. *Nat. Electron.* **2020**, *3*, 280–289. [CrossRef]
25. Rothschild, A.; Komem, Y. The Effect of Grain Size on the Sensitivity of Nanocrystalline Metal-Oxide Gas Sensors. *J. Appl. Phys.* **2004**, *95*, 6374–6380. [CrossRef]
26. Ji, H.; Zeng, W.; Li, Y. Gas Sensing Mechanisms of Metal Oxide Semiconductors: A Focus Review. *Nanoscale* **2019**, *11*, 22664–22684. [CrossRef] [PubMed]
27. Gaskov, A.; Rumyantseva, M.; Marikutsa, A. 7- Tin Oxide Nanomaterials: Active Centers and Gas Sensor Properties. *Tin Oxide Mater.* **2020**, 163–218. [CrossRef]

Disclaimer/Publisher's Note: The statements, opinions and data contained in all publications are solely those of the individual author(s) and contributor(s) and not of MDPI and/or the editor(s). MDPI and/or the editor(s) disclaim responsibility for any injury to people or property resulting from any ideas, methods, instructions or products referred to in the content.